Mon. Not. R. Astron. Soc. **000**, 000–000 (0000) Printed 9 February 2015 (MN LATEX style file v2.2)

Mid-infrared spectroscopy of the Andromeda galaxy

D. Hemachandra[1⋆], P. Barmby[1], E. Peeters[1,2], S.P. Willner[3], M.L.N. Ashby[3], H.A. Smith[3], K.D. Gordon[4], D.A. Smith[4], and G.G. Fazio[3]
[1] *Department of Physics and Astronomy, University of Western Ontario, London, ON, N6A 3K7, Canada*
[2] *SETI Institute, 189 Bernardo Avenue, Suite 100, Mountain View, CA 94043, USA*
[3] *Harvard-Smithsonian Center for Astrophysics, Cambridge, MA 02138, USA*
[4] *Space Telescope Science Institute, 3700 San Martin Drive, Baltimore, MD 21218, USA*

ABSTRACT

We present *Spitzer*/Infrared Spectrograph 5–21 μm spectroscopic maps towards 12 regions in the Andromeda galaxy (M31). These regions include the nucleus, bulge, an active region in the star-forming ring, and 9 other regions chosen to cover a range of mid-to-far-infrared colours. Our observations did not reproduce the suppressed 6–8 μm features and enhanced 11.3 μm feature intensity and FWHM seen with the ISOCAM instrument on the Infrared Space Observatory. In line with previous results, PAH feature ratios (6.2 μm and 7.7 μm features compared to the 11.2 μm feature) measured from our extracted M31 spectra, except the nucleus, strongly correlate. The equivalent widths of the main PAH features decrease with increasing radiation hardness, consistent with that observed for other nearby spiral and starburst galaxies. The nucleus does not show any PAH emission but does show strong silicate emission at 9.7 μm. Furthermore, different spectral features (11.3 μm PAH emission, silicate emission and [NeIII] 15.5 μm line emission) have distinct spatial distributions in the nuclear region: the silicate emission is confined towards the nuclear centre (19–27pc) while the PAH emission peaks 15″north of the centre. At this position, the PAH emission is atypical with strong emission at 11.2 μm and at 15-20 μm but suppressed emission at 6–8 μm. We also find that the silicate emission profile is redshifted and broader compared to that observed towards the Galactic centre. Both the silicate emission and atypical PAH emission provide evidence for a low luminosity active galactic nucleus in M31.

Key words: galaxies: individual: M31 – galaxies: ISM – galaxies: nuclei – infrared: ISM – ISM: molecules – ISM: lines and bands

1 INTRODUCTION

Mid-infrared spectra provide a unique diagnostic tool to understand the physical conditions in the interstellar medium of galaxies. The rich range of spectral features (Polycyclic Aromatic Hydrocarbons (PAHs), atomic fine structure lines (e.g. Ne, S) and the amorphous silicate feature centred at 9.7 μm) provide information on dust properties, radiation field and star formation. With the advent of infrared space telescopes, such as the Infrared Space Observatory (ISO, Kessler et al. 1996) and the *Spitzer* Space Telescope (Werner et al. 2004), mid-infrared spectroscopy has become an important method of investigating the infrared emission from galaxies.

PAHs are known as the main carrier of the ubiquitous mid-infrared emission bands (e.g. Allamandola et al. 1989, Puget & Leger 1989). They are large hydrocarbon molecules consisting of ∼50–100 carbon atoms (Tielens 2008). The main PAH features are seen at 3.3, 6.2, 7.7, 8.6, 11.3 and 12.7 μm (e.g., Gillett et al. 1973, Geballe et al. 1985, Peeters 2011). These bands are attributed to the vibrational de-excitation of PAH molecules through bending and stretching modes of C-H and C-C bonds (e.g. Allamandola et al. 1989, Puget & Leger 1989). The 6 to 8 micron features are thought to originate mostly from ionized PAHs and the 3.3 and 11.3 μm emission bands from neutral PAHs (e.g. Hudgins & Allamandola 2004 and reference therein, Hony et al. 2001, Galliano et al. 2008b).

The relative strength of the PAH features vary spatially within extended objects and from galaxy-to-galaxy (e.g. Galliano et al. 2008b). While extinction does influence the individual PAH bands to different degrees (e.g. Brandl et al. 2006; Stock et al. 2013), the observed spread in PAH intensity ratios is dominated by the PAH charge balance

⋆ E-mail: dhemacha@uwo.ca

(Galliano et al. 2008b). In addition, feature ratios do change more drastically close to active galactic nuclei where the overall strength of PAH emission also gets weaker (Roche et al. 1991, Smith et al. 2007b). Smith et al. (2007b) found that the mid-infrared spectra from some weak AGNs show suppressed 6 to 8 μm PAH features (by up to a factor of 10 in strength) but are bright at 11.3 μm. One possible explanation for this behaviour is that AGNs alter the grain composition by selective destruction of small PAHs and/or even can excite the PAHs. Alternatively, the PAH emission is modified by the low star formation intensity in the centers of many AGNs (Smith et al. 2007b).

Previous studies of nearby galaxies indicate that metallicity and radiation hardness can both affect the PAH emission (e.g. Madden 2000, Beirão et al. 2006, Engelbracht et al. 2008, Muñoz-Mateos et al. 2009). In particular, the PAH equivalent widths (EQWs) in nearby galaxies decrease with increasing radiation hardness, although Brandl et al. (2006) found no such correlation within their starburst sample. In addition, PAH EQWs show an anti-correlation with metallicity in star-forming galaxies. This variation of PAHs among galaxies has also been observed within H II regions of M101 (Gordon et al. 2008). But there are no other investigations done on a single star-forming galaxy with sufficiently high resolution to see whether the correlations mentioned above hold within a galaxy similar to the Milky Way.

The amorphous silicate feature at 9.7 μm is another aspect of the mid-infrared spectra of galaxies and in particular their nuclei. Spoon et al. (2007) classified infrared galaxies based on the equivalent width of the 6.2 μm PAH feature and the strength of the 9.7 μm silicate feature. They found galaxies spread along two distinct branches: one in which silicate absorption strength was anti-correlated with PAH equivalent width, and another in which the weak silicate feature strength did not depend on the 6.2 μm equivalent width. Silicate *emission* at 9.7 μm has also been observed towards several galaxies including LINERS, Seyfert galaxies, ULIRGs, and QSOs (e.g. Sturm et al. 2005; Hao et al. 2005; Spoon et al. 2007; Mason et al. 2012) and can be used to constrain the geometry and structure of the emitting nuclear region (Mason et al. 2009).

M31 with its proximity (785 ± 25 kpc; McConnachie et al. 2005) and rich observational databases provides the most detailed view of a star forming galaxy similar to the Milky Way. The active star forming ring visible in 8 μm *Spitzer*/IRAC images (Barmby et al. 2006) provides evidence of abundant PAHs in M31. However, ISOCAM spectro-imaging observations of M31(Cesarsky et al. 1998) showed that four regions including the nucleus and bulge of this galaxy have very odd PAH spectra, bright at 11.3 μm while showing weak or no 6.2, 7.7, and 8.6 μm bands. Investigating this unusual PAH emission was the main motivation for the work described in this paper. The centre of M31 has a complicated physical structure. It hosts a very inactive supermassive black hole with a mass of $0.7-1.4\times10^{8}$ $M_{\odot}$ (Bacon et al. 2001; Bender et al. 2005) and also has a lopsided nuclear disk with two stellar components (Lauer et al. 1993) and an A-star cluster (Bender et al. 2005). While M31's nucleus is known to be inactive from an X–ray perspective (Li et al. 2011), mid-infrared indicators of its nuclear activity, such as infrared excess or spectral features of silicates, have received relatively little attention. The higher spatial resolution available in observations of a very nearby galaxy like M31, compared to luminous, distant objects such as ultra-luminous infrared galaxies (Spoon et al. 2007) or nearby Seyferts (Mason et al. 2009), makes exploring its mid-infrared spectrum worthwhile.

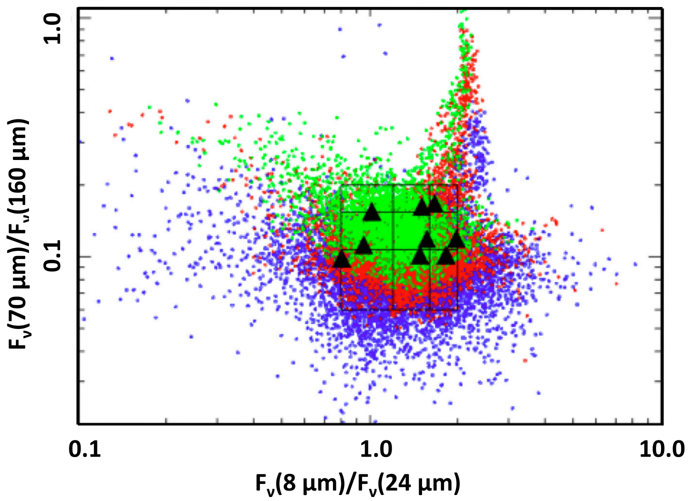

Figure 1. $8-24/70-160$ μm colour-colour diagram of M31 obtained from IRAC and MIPS imaging. Colour-coding of points represents 24 μm flux, from faintest (blue) to brightest (red). The plot is divided into 9 regions (black grid), and the observations were made to cover those regions subject to a 24 μm brightness cut. The black triangles indicate colours of the regions we observed.

We employed mid-infrared spectral maps from the *Spitzer*/Infrared Spectrograph (IRS) from 12 regions of M31 for a further investigation of its infrared properties. This sample includes the nucleus, bulge, an active region in the star-forming ring (all previously observed by ISOCAM), and 9 other regions chosen to cover a range of properties as described in Section 2.1. We obtained the processed version of ISOCAM observations of M31 and compare them with the IRS results in Section 3.1. Section 4.1 discusses PAH intensity ratios. In Section 4.2, we investigate the relationship between PAH equivalent widths and radiation hardness and compare to that found by Engelbracht et al. (2008) and Gordon et al. (2008). Metallicity and PAH EQWs are compared in Section **??**, and Section 5 discusses the dust properties of the nucleus. The paper is summarized in Section 6.

2 OBSERVATIONS AND DATA REDUCTION

2.1 IRS observations

We obtained mid-infrared spectral maps of 12 regions in M31 using the *Spitzer*/IRS instrument (Houck et al. 2004) covering wavelengths from 5 to 21 microns. A background observation was also made off the galaxy along the minor axis for use in background subtraction from the data cubes. The 12 target regions include the nucleus, the 'bulge' and 'active' regions previously observed by ISOCAM (the latter is Region 9 in our sample), and 9 other regions selected to cover a range of metallicities and dust temperatures.[1] These 9 regions were chosen by convolving the IRAC 8 μm (Barmby et al. 2006) and MIPS (Gordon et al. 2006) maps to the same resolution and constructing an $8-24/70-160$ μm colour-colour diagram (Figure 1). This colour space was used to give a rough definition of the types of spectral energy distribution; the dense region in the plot was split into a 3x3 grid and one pixel in each grid region (subject to a 24μm brightness cut) was selected for spectroscopy. The locations of the observed regions are shown in Figure 2, and their coordinates and metallicities are given in Table 1. Except for regions 5 and 8, all of our mapped regions contain an H II region with an optical spectroscopic metallicity measurement by Sanders et al. (2012); Table 1 gives the measurements from the method Sanders et al. (2012) denote "N06 N2" (Nagao et al. 2006). For regions 5 and 8 we estimated metallicities using the M31 radial gradient that Sanders et al. (2012) fit to the HII region "N06 N2" measurements: $12 + \log[\mathrm{O/H}] = 9.09 - 0.00195R\mathrm{gc}$.

For our observations we used the IRS Short-Low (SL) and Long-Low (LL) modules, which cover wavelengths from 5 to 21 microns. The Low modules have resolving power in the range 60–130. Each low-resolution module is divided into two sub-slits which provide spectroscopy in either first or second order. They are denoted as SL1 (7.5–14.5 μm), SL2 (5.2–7.6 μm), LL1 (20.5–38.5 μm, not used in these observations), and LL2 (14.5–20.75 μm). All M31 regions were observed in September 2007 as part of G. G. Fazio's Guaranteed Time (program ID 40032). The map size was based on the size of the IRS slits (SL: $3.6'' \times 57''$, LL: $10.5'' \times 168''$). Each region was covered by 18 overlapping observations of the SL slit and 11 overlapping observations of the LL slit making the map size $32'' \times 57''$ for SL and $58'' \times 168''$ for LL. Figure 3 shows an example of the slit arrangement. For the brighter regions (nucleus, bulge), ramp times of 14 s (SL) and 30 s (LL) were used, while for the fainter regions, ramp times of 60 and 120 s were used respectively. Background observations were taken with each module (2 per ramp time). Because all of the targets are in the same part of the sky, a common background observation was used for multiple targets to subtract the background emission.

2.2 IRS Data Reduction

The data were reduced through the SSC pipeline (ver. S17.2.0), and the maps were assembled using the CUBISM program (Smith et al. 2007a). Bad pixel removal was also done using CUBISM, and the background observations were used to subtract the background emission from these cubes following the method outlined by Gordon et al. (2008). Spectra were extracted using a $30'' \times 50''$ rectangular aperture, which corresponds to 114×190 pc at the distance of M31. The aperture size was selected to cover the overlapping area of the SL and LL modes; all the IRS maps cover more area than considered here. In order to study the spatial variation of the emission near the nucleus, we also extracted spectra

[1] One additional spectral map in M31 is available in the *Spitzer* archive (AOR key 12019200); unfortunately it does not cover the 5–13 μm region, which is the major focus of this paper. We therefore elected to not include these observations.

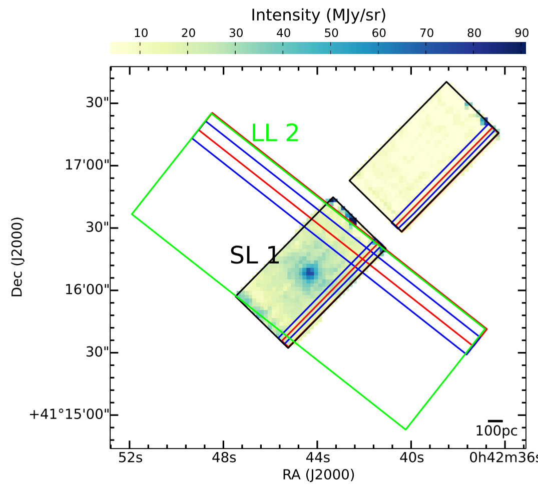

Figure 3. The 7.6 μm plane constructed from the SL1 data cube of the nucleus, showing the arrangement of slits used to cover the region. Black boxes outline the footprint of the SL1 maps (the off-center SL1 map is from observations made when SL2 was centred) and the green box outlines the LL2 map. Blue and red slits show how each map was covered using overlapping slit positions.

from two smaller regions within that map; these will be further discussed in Section 5. The spectrum of NGC 206 is very noisy and was removed from our analysis.

There is wavelength overlap between the SL1 and SL2 spectra and also between the SL1 and LL2 spectra. To generate a single spectrum for each M31 region it is necessary to combine the spectra and account for photometric offsets between them. Such offsets are commonly seen in IRS spectra extracted from extended regions, since the slit loss is not well-characterized (**Els please check this sentence**). The SL1 and SL2 flux densities were generally quite well-matched over the wavelength overlap region ($7.5 < \lambda < 7.6\mu$m) and those two orders were combined by averaging fluxes over the overlap region. In cases with offsets between SL1 and SL2, we determined the flux offset by comparing SL1 to the 'bonus order SL3' and then SL1+3 to SL2. We combined the extracted SL1 and SL3 spectra by computing the average flux densities over the overlap region and adding a constant to the SL1 spectra so that they matched the SL3 average. The SL1 and SL2 orders were then combined as described above. After this procedure there was still a noticeable mis-match between the SL and LL spectra. We addressed this by scaling the SL spectra to match IRAC 8 μm fluxes as follows. IRAC fluxes were measured on the 8 μm image (Barmby et al. 2006) in the same apertures used to extract the IRS spectra. An extended source aperture correction of 0.824 was applied to the IRAC fluxes; this value was computed using the formula in the IRAC Data Handbook () with the radius of a circular aperture having the same area as the extraction aperture. The *Spitzer* synthetic photometry software (Spitzer Science Center 2012) was then used to quantify the colour correction for each spectrum, i.e. the multiplicative factor K between the IRAC photometry over its broad bandpass and the IRS flux density at the centre of the bandpass. For each spectrum we computed the additive offset between the color-corrected IRS flux density and

Table 1. Spitzer/IRS Target Locations in M31

Name	R.A. (J2000)	Decl. (J2000)	$R_{gc}{}^{b}$	$12 + \log(O/H)^{c}$
Nucleus[a]	$00^{h}42^{m}44\overset{s}{.}31$	$41°16'09\overset{''}{.}4$	0.0	
Bulge[a]	$00^{h}42^{m}35\overset{s}{.}00$	$41°21'01\overset{''}{.}0$	4.7	8.90 ± 0.03
Region 1	$00^{h}41^{m}30\overset{s}{.}41$	$40°43'07\overset{''}{.}8$	12.4	9.20 ± 0.20
Region 2	$00^{h}45^{m}22\overset{s}{.}85$	$41°38'53\overset{''}{.}1$	13.0	9.07 ± 0.02
Region 3	$00^{h}40^{m}37\overset{s}{.}37$	$41°01'29\overset{''}{.}4$	12.1	8.85 ± 0.01
Region 4	$00^{h}41^{m}17\overset{s}{.}86$	$41°07'09\overset{''}{.}8$	8.7	8.89 ± 0.06
Region 5	$00^{h}43^{m}39\overset{s}{.}57$	$41°19'03\overset{''}{.}1$	7.0	8.93 ± 0.08
Region 6	$00^{h}43^{m}35\overset{s}{.}72$	$41°23'15\overset{''}{.}0$	4.3	8.73 ± 0.08
Region 7	$00^{h}40^{m}53\overset{s}{.}98$	$40°58'58\overset{''}{.}9$	8.7	8.40 ± 0.08
Region 8	$00^{h}42^{m}21\overset{s}{.}60$	$41°07'17\overset{''}{.}4$	3.1	8.94 ± 0.08
Region 9[a]	$00^{h}41^{m}00\overset{s}{.}00$	$40°36'20\overset{''}{.}3$	13.5	8.86 ± 0.02
NGC 206	$00^{h}40^{m}20\overset{s}{.}20$	$40°44'54\overset{''}{.}0$	9.8	
Background	$00^{h}44^{m}41\overset{s}{.}80$	$40°58'56\overset{''}{.}0$	29.5	

[a]Regions with ISOCAM data.
[b]De-projected galactocentric distance in kpc.
[c]Metallicities from Sanders et al. (2012), except for Regions 5 and 8 where metallicities are estimated from the radial metallicity profile.

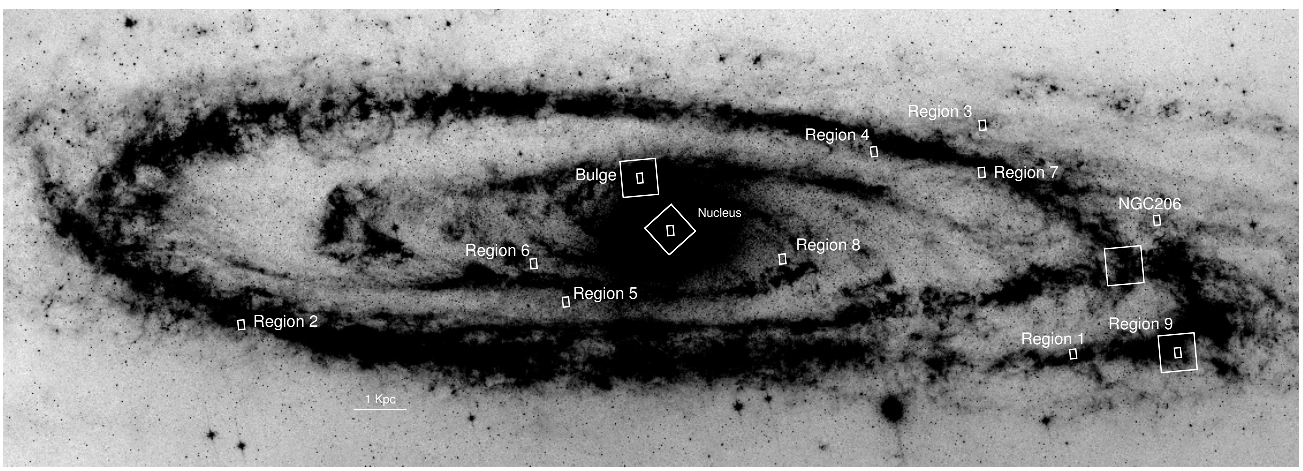

Figure 2. An 8 micron negative IRAC image of M31 (Barmby et al. 2006). Small white rectangles ($30'' \times 50''$) show the regions that we observed, and larger squares ($192'' \times 192''$) show the regions observed by Cesarsky et al. (1998).

the IRAC aperture-corrected flux density, and used this to correct the SL spectra; this method was also used by Sandstrom et al. (2012). Although a multiplicative offset could also have been used to match the IRS photometry to IRAC, the resulting change in spectral slope increased the size of the SL/LL offset. The SL spectra corrected with additive offsets were closely-matched to the LL spectra, and the final combination of SL and LL was done using the average-and-offset procedure described above for SL1 and SL3.

2.3 ISOCAM Data Reduction

To compare our results with those of Cesarsky et al. (1998), we retrieved the highly processed ISOCAM data provided by Boulanger et al. (2005) for the nucleus, bulge, and region 9. The ISOCAM data were obtained with the circular variable filters (CVFs) over a $3' \times 3'$ field of view at a scale of $6''$ per pixel. The wavelength range covered was 5.15–16.5 μm at a resolution of $\lambda/\Delta\lambda \approx 45$; the ISOCAM instrument is described by Cesarsky et al. (1996). An example image of the ISOCAM data is shown in Figure 4. For the three regions, we extracted spectra using the same $30'' \times 50''$ aperture as for the IRS data.

3 SPECTRAL CHARACTERISTICS AND FEATURE MEASUREMENTS

The final processed IRS spectra are shown in Figure 5, except for the nucleus, discussed in Section 5. All of the main PAH features, including the 6.2, 7.7, 8.6 and 11.3 μm bands, are clearly visible for all the regions shown here. The IRS spectra also show atomic line emission such as [Ar II], [Ar III], [S III], [S IV], [Ne II], [Ne III] and molecular H_2 emission at 12.3 μm. Some of the spectra display a contribution to the continuum from starlight emission.

3.1 ISOCAM versus IRS

As mentioned in the Introduction, based on ISOCAM observations of four regions in M31, Cesarsky et al. (1998) re-

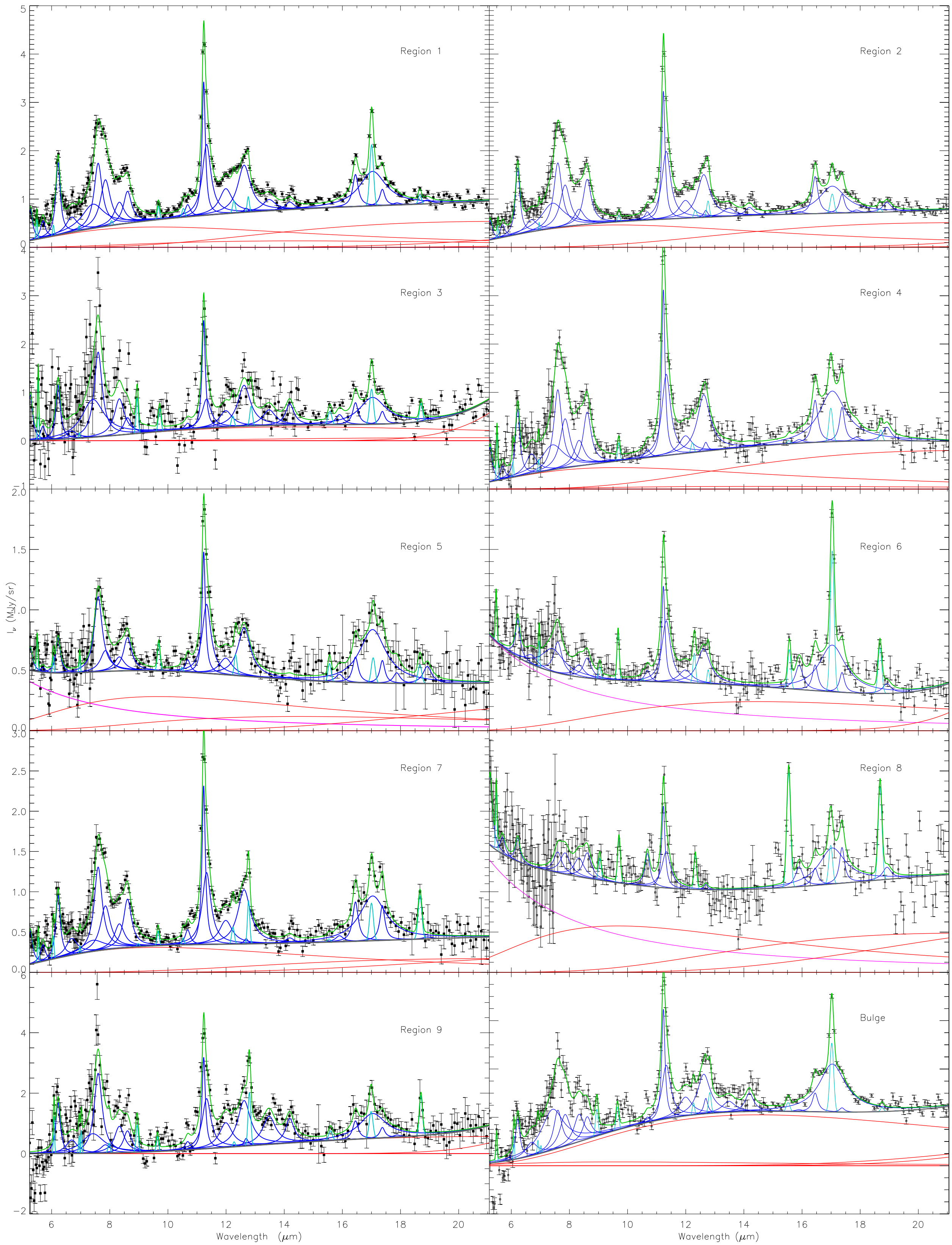

Figure 5. Observed IRS spectra and detailed PAHFIT decompositions (see Section 3.2). Regions are labeled in each panel. Black squares show the observed data, and red, blue, light blue, pink and green lines represent the modelled dust continua, PAH features, atomic lines, starlight continuum and the fit respectively. The black line shows the total modelled continuum. Vertical scales differ in different panels. Spectra from the nucleus and NGC 206 are not shown here.

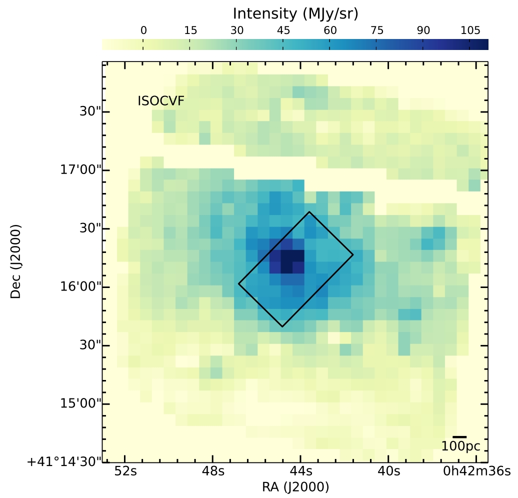

Figure 4. 11.3 μm negative image (dark colours indicate higher flux) of the ISOCAM data cube from the nucleus of M31. The black box shows the size of the aperture ($30'' \times 50''$) used to extract spectra.

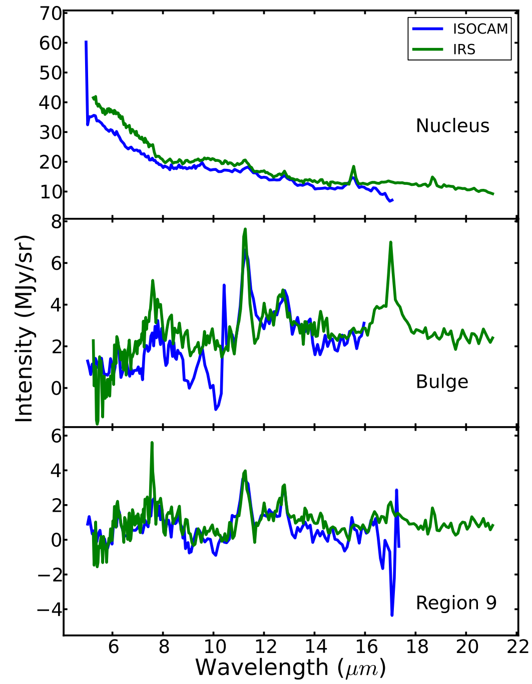

Figure 6. Comparison of IRS and re-processed ISOCAM spectra for the Nucleus (top), Bulge (middle) and Region 9 (bottom) in M31.

ported suppression of the common 6–8 μm PAH bands and a strong 11.3μm PAH band. The 11.3 μm band profile was found to vary from region to region. In addition, Pagani et al. (1999) confirmed that the star-forming ring in M31 shows very weak PAH emission in the 6 to 8 μm region. However, the IRS spectra presented here, except the nucleus, do not show such unusual behaviour (Figure 5). Indeed all regions, except the nucleus, show a normal mid-infrared spectrum similar to other nearby starforming galaxies.

Until 2005, ISOCAM-CVF data were not properly background subtracted and they were contaminated with zodiacal emission and stray light. Differential spectra between regions of relatively strong and weak emission were previously used to overcome this problem (more details about the differential spectra are given by Cesarsky et al. 1998, Pagani et al. 1999). In 2005, all ISOCAM-CVF data were reprocessed and corrected for the zodiacal emission (Boulanger et al. 2005). We obtained newly-processed ISOCAM spectra from three regions in our IRS sample (see Section 2.3) in order to compare them with the corresponding IRS spectra. Figure 6 shows that although the relative feature intensities in the IRS and ISOCAM spectra differ in detail, the spectral shapes are almost identical; the re-processed ISOCAM data do not agree with the previous differential spectra. Neither the bulge nor Region 9 shows any depletion in 6 to 8 μm features as described by Cesarsky et al. (1998). The new ISOCAM reduction appears to eliminate the discrepancies between ISOCAM and IRS, resulting in less 'strange' infrared spectra for M31. For the remainder of this work, we discuss only the IRS spectra.

3.2 PAHFIT

The PAH features in IRS spectra are often blended with neighbouring PAH features and atomic lines. Therefore measuring the strength of PAH features is difficult. To achieve this task a tool called PAHFIT, introduced by Smith et al. (2007b), was used. PAHFIT is an IDL based tool designed for decomposing *Spitzer* IRS low-resolution spectra of PAH emission sources. PAHFIT uses six main components to fit the surface brightness. These are starlight continuum, featureless thermal dust continuum, pure rotational lines of H_2, fine-structure lines, dust emission features and dust extinction. The starlight is represented by blackbody emission at a fixed temperature of 5000 K, and the dust continuum is represented by 8 modified blackbodies (emissivity proportional to ν^2) at fixed temperatures of 35, 40, 50, 65, 90, 135, 200, and 300 K. The final fit obtained with PAHFIT does not necessarily use all eight dust components. The infrared extinction is considered as a combination of a power law plus silicate absorption features with peaks at 9.7 and 18 μm. Line features are represented by Gaussian profiles with widths set by the instrumental resolution and dust features are represented by Drude profiles; more details about PAHFIT are given by Smith et al. (2007b).

Initial attempts at fitting the spectra with PAHFIT showed that some components were negligible, and to avoid over-fitting we re-ran the fits without these components. None of the IRS spectra shows significant silicate absorption around 9.7 or 18 μm, and the extinction calculated by PAHFIT was almost zero for all the initial fits. Except for four regions (the bulge, Region 5, Region 6 and Region 8), the starlight contribution is also negligible. We adjusted the PAHFIT input parameters to fix extinction to zero for all regions and starlight to zero for all but the four regions above. Typically only two or three thermal dust components had significant power in our fits, but we did not fix the unused components to zero. Regions 3 and 9 were found to have very low dust continuum emission compared to other spectra, possibly because of noisy data at short wavelengths. However the other features in these spectra appear to be fit correctly. The spectrum of the nucleus shows silicate emission, which is not included in PAHFIT; our modifications of PAHFIT to analyze this spectrum are discussed in see Section 5.

3.3 PAH features

PAHFIT returns fluxes and equivalent widths (EQWs) of PAH features, which are given in Tables 2 and 3. For easier comparison with previous work, the tables give measurements for the 7.7, 11.3, 12.7 and 17.0 μm PAH complexes as defined by Smith et al. (2007b), as computed from the individual constituent features measured by PAHFIT. The intensities of the features do not include any contribution from the continuum, but the equivalent width computed by

$$\mathrm{EQW} = \int \frac{I_{\nu,\mathrm{feature}}}{I_{\nu,\mathrm{cont}}}\, d\lambda, \tag{1}$$

is a measure of the ratio of the continuum emission ($I_{\nu,\mathrm{cont}}$) to the line strength ($I_{\nu,\mathrm{feature}} = I_\nu = -I_{\nu,\mathrm{cont}}$). The continuum emission is mainly from dust grains, much larger than PAH molecules. Hence, by studying EQWs of PAHs, we can study how the PAHs compete with the dust grains in the mid-infrared wavelengths. PAHFIT returns the EQWs for each PAH feature, we calculated the uncertainties using a Monte-Carlo method. In that method, for each region, PAHFIT was run 500 times on randomly generated data points normally distributed within the uncertainties of the spectrum. PAHFIT returned 500 EQWs for each PAH feature, and the standard deviation of EQWs for a given feature was taken as its uncertainty. The EQWs from Regions 3 and 9 were removed from further analysis because the negligible dust continuum for these spectra makes the EQWs highly uncertain.

3.4 Atomic line features

PAHFIT also returns the line strengths and uncertainties for atomic lines, listed in Table 4. Not all lines were detected by PAHFIT, so we calculated upper limits for non-detected lines.[2] Line ratios of [Ne III]/[Ne II] and [S IV]/[S III] 18 have been used as an indication of the radiation hardness, and Engelbracht et al. (2008) defined a combination of these two line ratios as a 'radiation hardness index (RHI)':

$$\mathrm{RHI} = \left(\log \frac{[\mathrm{Ne\ III}]}{[\mathrm{Ne\ II}]} + \left[0.71 + 1.58 \log \frac{[\mathrm{S\ IV}]}{[\mathrm{S\ III}]} \right] \right) /2 \tag{2}$$

Here, 1.58 and 0.71 are the slope and intercept of the [Ne III]/[Ne II] vs [S IV]/[S III] plot (Figure 7) for the starburst sample from Engelbracht et al. (2008). Figure 7 compares the atomic line emission from the selected regions of M31 to the starburst galaxy sample; although none of our spectra have detections of all four lines, our limits are mostly

[2] To find the upper limits for the flux of missing atomic lines, we assumed the line to be a Gaussian profile with a FWHM as given by PAHFIT. The peak intensity was taken to be 3 times the RMS, where RMS is the root mean square of the noise at the position of a missing line.

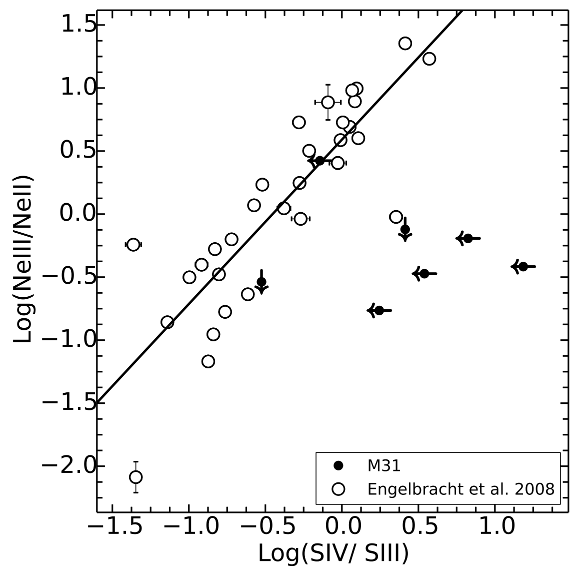

Figure 7. Log([Ne III]/[Ne II]) vs log([S IV]/[S III]) for the M31 regions in our sample (black dots) and the starburst sample from Engelbracht et al. (2008) (open dots). The straight line is the line of best fit for the starburst sample. Upper limits are 3σ.

consistent with the trend. To compute RHI in the case of missing lines, we compute the term in equation 3.4 for which both lines are detected and use this to estimate a value for the other term via the best-fit line. Regions 2, 5, and 8 had detections of only one line per element, so we used the appropriate upper limits to calculate RHI for these spectra (**not sure I have done this correctly yet**).

4 RESULTS: EXTRANUCLEAR REGIONS

4.1 PAH band ratios

Both the 6.2 and 7.7 μm features are thought to be coming from ionized PAHs and the 11.3 μm feature from neutral PAHs. Therefore we expect to see a correlation between the intensities of 6.2 and 7.7 μm PAH features normalized by the 11.3 μm feature. Figure 8 compares the PAH flux ratios of 7.7/11.3 and 6.2/11.3 features. The figure shows a good correlation between these two PAH line ratios, consistent with that of the SINGS sample shown by Smith et al. (2007b). A similar correlation was also reported by Galliano et al. (2008b) for a sample of galaxies and a handful of extended HII regions and by Vermeij et al. (2002) for Galactic and Magellanic Cloud HIIregions. This provides evidence that the PAH emission from M31 is not unusual.

4.2 PAH equivalent widths versus radiation hardness and metallicity

As mentioned in the introduction, PAH equivalent widths tend to decrease as radiation hardness increases, and as metallicity decreases (Calzetti et al. 2010). Figures 9 and 10 show the equivalent widths of the 8 μm feature (a combination of the 7.7, 8.3 and 8.6 μm PAHFIT components)

Table 2. PAH Emission Line Strengths[a]

Region	5.7 μm	6.2 μm	7.7 μm[b]	8.3 μm	8.6 μm	10.7 μm	11.3 μm[b]	12.0 μm	12.7 μm[b]	17.0 μm[b]
Bulge	...	1.32 ± 0.08	7.7 ± 0.6	1.1 ± 0.2	0.7 ± 0.1	0.07 ± 0.03	1.85 ± 0.08	0.49 ± 0.05	1.02 ± 0.09	1.39 ± 0.04
Region 1	0.36 ± 0.05	1.20 ± 0.04	3.8 ± 0.2	0.46 ± 0.04	0.50 ± 0.03	0.08 ± 0.01	1.18 ± 0.02	0.32 ± 0.02	0.54 ± 0.02	0.58 ± 0.02
Region 2	0.27 ± 0.03	1.10 ± 0.03	3.7 ± 0.2	0.33 ± 0.04	0.70 ± 0.03	0.053 ± 0.008	1.13 ± 0.02	0.23 ± 0.01	0.51 ± 0.03	0.51 ± 0.02
Region 3	0.3 ± 0.1	0.9 ± 0.1	3.9 ± 0.6	0.7 ± 0.1	0.3 ± 0.1	...	0.68 ± 0.07	0.21 ± 0.05	0.47 ± 0.07	0.45 ± 0.04
Region 4	0.14 ± 0.04	0.56 ± 0.03	2.1 ± 0.2	0.26 ± 0.04	0.41 ± 0.03	0.029 ± 0.008	0.70 ± 0.02	0.12 ± 0.01	0.31 ± 0.02	0.44 ± 0.02
Region 5	...	0.24 ± 0.04	0.79 ± 0.07	0.12 ± 0.04	0.21 ± 0.03	0.032 ± 0.008	0.45 ± 0.02	0.09 ± 0.01	0.22 ± 0.01	0.33 ± 0.04
Region 6	...	0.26 ± 0.03	0.8 ± 0.2	0.10 ± 0.03	0.13 ± 0.03	0.029 ± 0.008	0.38 ± 0.02	0.07 ± 0.01	0.16 ± 0.01	0.29 ± 0.02
Region 7	0.21 ± 0.03	0.62 ± 0.03	2.0 ± 0.2	0.30 ± 0.04	0.45 ± 0.03	0.058 ± 0.008	0.77 ± 0.02	0.18 ± 0.01	0.37 ± 0.03	0.47 ± 0.04
Region 8	...	0.09 ± 0.04	0.22 ± 0.07	0.09 ± 0.04	0.10 ± 0.03	0.051 ± 0.009	0.16 ± 0.02	...	...	0.15 ± 0.02
Region 9	...	1.3 ± 0.1	4.4 ± 0.6	0.9 ± 0.1	0.5 ± 0.1	0.09 ± 0.03	1.32 ± 0.07	0.51 ± 0.05	0.83 ± 0.07	0.6 ± 0.1

[a] Units are 10^{-15} W m^{-2}.
[b] PAH complexes, as described in text.

Table 3. PAH Emission Line Equivalent Widths[a]

Region	5.7 μm	6.2 μm	7.7 μm[b]	8.3 μm	8.6 μm	10.7 μm	11.3 μm[b]	12.0 μm	12.7 μm[b]	17.0 μm[b]
Bulge	...	1.2 ± 0.2	4.1 ± 0.4	0.51 ± 0.07	0.30 ± 0.06	0.03 ± 0.01	0.78 ± 0.04	0.22 ± 0.02	0.49 ± 0.05	1.16 ± 0.04
Region 1	0.39 ± 0.08	1.2 ± 0.1	3.4 ± 0.3	0.43 ± 0.04	0.47 ± 0.04	0.09 ± 0.01	1.45 ± 0.04	0.43 ± 0.03	0.76 ± 0.04	1.26 ± 0.05
Region 2	0.28 ± 0.04	1.02 ± 0.06	3.4 ± 0.2	0.32 ± 0.04	0.70 ± 0.04	0.07 ± 0.01	1.58 ± 0.04	0.35 ± 0.02	0.85 ± 0.05	1.33 ± 0.06
Region 3	4.3 ± 2.3	8.3 ± 2.3	18.5 ± 4.2	2.8 ± 0.8	0.9 ± 0.5	...	2.1 ± 0.3	0.7 ± 0.2	1.6 ± 0.3	2.4 ± 0.3
Region 4	0.28 ± 0.09	1.0 ± 0.1	3.7 ± 0.4	0.48 ± 0.07	0.77 ± 0.07	0.07 ± 0.02	1.67 ± 0.06	0.31 ± 0.04	0.82 ± 0.06	1.65 ± 0.08
Region 5	...	0.12 ± 0.03	0.61 ± 0.07	0.10 ± 0.03	0.20 ± 0.03	0.05 ± 0.01	0.77 ± 0.04	0.17 ± 0.03	0.50 ± 0.04	1.6 ± 0.2
Region 6	...	0.10 ± 0.04	0.6 ± 0.2	0.10 ± 0.04	0.14 ± 0.03	0.05 ± 0.01	0.77 ± 0.05	0.15 ± 0.03	0.42 ± 0.05	1.7 ± 0.1
Region 7	0.32 ± 0.05	0.86 ± 0.06	2.2 ± 0.1	0.44 ± 0.06	0.69 ± 0.06	0.12 ± 0.02	1.81 ± 0.07	0.48 ± 0.05	1.08 ± 0.09	2.2 ± 0.3
Region 8	...	...	0.10 ± 0.05	0.09 ± 0.04	0.10 ± 0.03	0.09 ± 0.02	0.30 ± 0.04	...	...	0.62 ± 0.08
Region 9	...	$(2.4 \pm 1.1) \times 10^2$	$(1.4 \pm 0.4) \times 10^2$	15.5 ± 5.6	7.9 ± 2.8	0.5 ± 0.2	6.8 ± 1.1	2.3 ± 0.6	3.5 ± 0.8	2.2 ± 0.8

[a] Units are μm.
[b] PAH complexes, as described in text.
Continuum for Regions 3 and 9 is very weak. Equivalent widths are highly uncertain and not considered in the analysis (see Section 3).

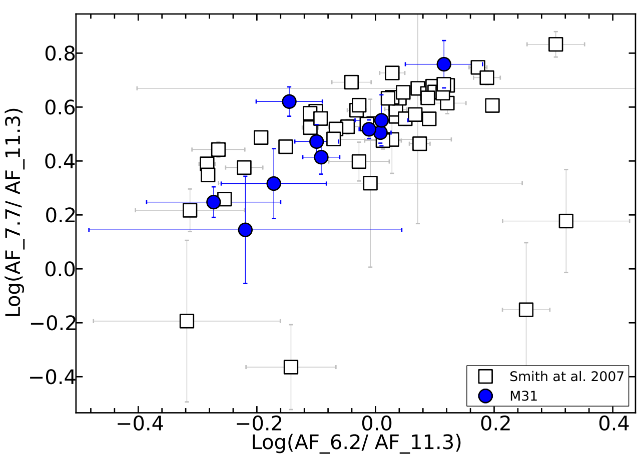

Figure 8. Ratios of PAH feature fluxes (7.7 μm/11.3 μm versus 6.2 μm/11.3 μm) for 10 regions in M31. Open squares represent the central regions of nearby galaxies as observed in the SINGS sample by Smith et al. (2007b).

and the 7.7 and 11.2 μm features as a function of RHI, with the starburst sample of Engelbracht et al. (2008) and H II regions in M101 (Gordon et al. 2008) for comparison. The M31 regions have about the same properties as the starburst galaxies and M101 HII regions, except for one M31 region with really high RHI (CHECK prob bad data) and one with really high EQW (CHECK). No clear trend is defined by the M31 data, unsurprising given the uncertainties and the limited number of regions. Figure 12 compares PAH EQWs versus metallicity for our sample and the starburst galaxies of Engelbracht et al. (2008) (see also alternate version using Gordon data instead). We do not have enough data from low-metallicity regions in M31 to observe the expected decrease of PAH EQW with decreasing metallicity; however the M31 data occupy the same region of parameter space as the M101 data and we conclude that the EQWs of the regions in M31 are consistent with previously published "normal" values. The M31 region with very low 7.7 μm equivalent widths is Region 8, which has a noisy spectrum in the blue as well as substantial modelled contribution from starlight (see Figure 5).

5 RESULTS: THE NUCLEAR REGION

Examining the *Spitzer*-IRS spectral data cube for the nuclear region, we noticed that different spectral features vary spatially within this region. The 11.2 μm PAH emission is discrete and patchy (Figure 13a). Indeed, the majority of the 11.2 μm PAH emission is from a region 15″ north of the nucleus (00:42:43.947, +41:16:22.92) and not from the nucleus itself. Weaker 11.2 μm PAH emission is also found near the edge of the map peaking at 00:42:45.497, +41:15:43.97 and near 00:42:45.869; +41:16:11.38. The locations of the two weaker 11.2 μm PAH emission peaks are also near positions exhibiting CO(2-1) line emission (#36 and 28 of Melchior & Combes 2013, the strongest 11.2 μm PAH emission peak is outside the CO FOV). On the other hand, the centre shows no PAH emission, but it does have silicate emission around

Table 4. Atomic Emission Line Strengths[a]

Region	[Ar II] 7.0 μm	[Ar III] 9.0 μm	[S IV] 10.5 μm	[Ne II] 12.8 μm	[Ne III] 15.5 μm	[S III] 18.7 μm
Bulge	< 0.12	0.17 ± 0.03	< 0.11	0.07 ± 0.01	0.025 ± 0.006	0.007 ± 0.003
Region 1	< 0.05	< 0.06	0.020 ± 0.004	0.020 ± 0.004	< 0.01	0.008 ± 0.001
Region 2	< 0.05	< 0.06	< 0.02	0.022 ± 0.004	< 0.01	0.003 ± 0.002
Region 3	< 0.15	0.09 ± 0.02	< 0.10	0.03 ± 0.01	0.020 ± 0.004	0.015 ± 0.003
Region 4	< 0.04	< 0.04	< 0.02	< 0.02	< 0.01	0.004 ± 0.002
Region 5	< 0.04	< 0.02	< 0.02	< 0.01	0.009 ± 0.004	0.008 ± 0.004
Region 6	0.02 ± 0.01	0.014 ± 0.007	< 0.01	< 0.01	0.019 ± 0.002	0.019 ± 0.002
Region 7	< 0.04	< 0.04	0.008 ± 0.003	0.035 ± 0.005	< 0.01	0.027 ± 0.004
Region 8	< 0.04	0.017 ± 0.006	< 0.02	< 0.01	0.041 ± 0.002	0.023 ± 0.002
Region 9	0.09 ± 0.04	0.12 ± 0.03	< 0.09	0.13 ± 0.01	< 0.04	0.05 ± 0.02

[a]Units are 10^{-15} W m^{-2}. Upper limits (3σ) are indicated with a $<$ mark.

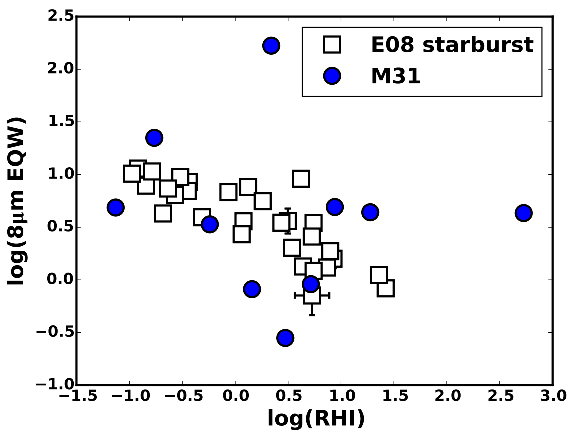

Figure 9. Equivalent width of the 8 μm PAH feature versus radiation hardness index (RHI) for the M31 sample (blue), and the starburst galaxy sample from Engelbracht et al. (2008) (open squares).

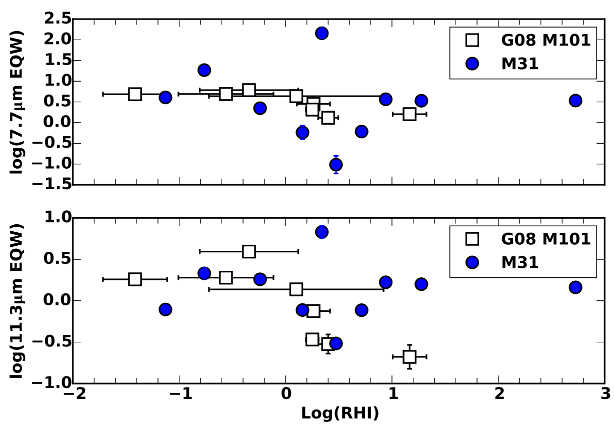

Figure 10. Equivalent widths of the 7.7 μm PAH feature (top panel) and 11.3 μm PAH feature (bottom panel) versus radiation hardness index (RHI) for the M31 sample. Open squares represent H II regions in M101 observed by Gordon et al. (2008).

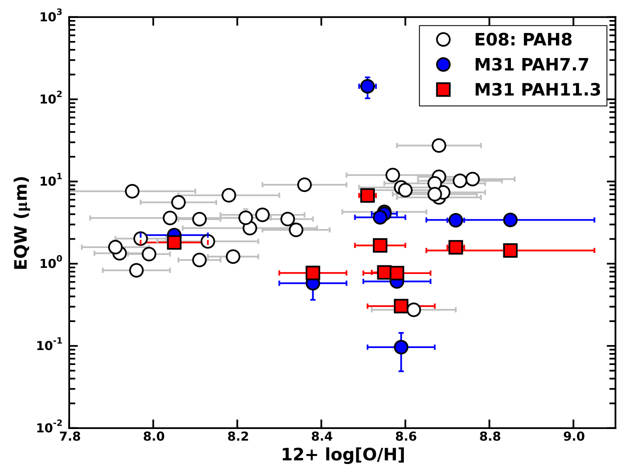

Figure 11. PAH equivalent widths versus metallicity. Filled circles are M31 7.7 μm EQWs; filled squares are M31 11.3 μm EQWs; open circles are 8 μm EQWs for the starburst sample from Engelbracht et al. (2008). Metallicities of the M31 regions have had 0.35 dex subtracted to account for the offset between direct and strong-line measurements.

9.7 μm, which comes only from the nucleus and is not present in the North region (Figure 13b).[3] Although [NeIII] 15.5 μm line emission is strong at the three locations with 11.2 μm PAH emission and weak(er) at the nucleus, it is also present across the nuclear region and thus distinct from that of the silicate and PAH emission.

Some structures seen in the optical near the M31 nucleus, such as the double nucleus and cluster of young stars, cannot be resolved with the data discussed here. The IRS spectral cubes have pixel sizes of $1''.8$, and the SL PSF FWHM is 2.5–3$''$depending on the wavelength, while the two components of the nucleus are separated by only $0''.5$ (Bender et al. 2005). However, the nuclear silicate emission and the north 11.2 μm PAH emission appear to be marginally spatially resolved: their radial profiles have full

[3] The spatial resolution and pixel scale of the ISOCAM data are not sufficient to resolve the centre and north regions.

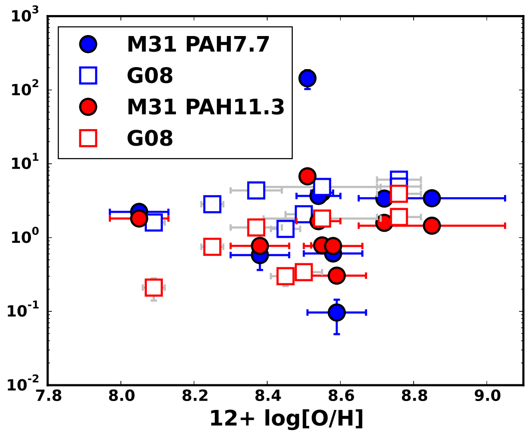

Figure 12. PAH equivalent widths versus metallicity. Filled circles are M31 EQWs; open squares are M101 EQWs from Gordon et al. (2008). Metallicities of the M31 regions have had 0.35 dex subtracted to account for the offset between direct and strong-line measurements.

widths at half maximum (FWHM) of 5–7$''$ (corresponding to 19–27pc). To examine the two regions in more detail, we extracted spectra from the centre and the North regions using $9'' \times 9''$ square apertures as shown in Figures 14, 15 and 16. Both spectra show a blue continuum and atomic fine-structure lines but they exhibit distinct dust emission consistent with the spatial maps: PAH emission is detected in the north spectrum while silicate emission is seen towards the nucleus.

Figure 14 (top) shows the results of PAHFIT applied to the spectrum of the north region. Atomic fine-structure lines of Ne and S are detected as well as H_2 emission at 17 μm. In addition, PAH emission is clearly detected at 11.3 μm and at 15-20 μm while it is weak or absent at 6–8 μm. We compared the PAH emission with that of the HII-type galaxy NGC0337 in Figure 14 (bottom). Despite the enhanced noise level at the shorter wavelengths, it is clear that the emission shortwards of 10 μm is atypical for PAHs but rather seem to exhibit a broad plateau from $\sim$6 to $\sim$7.5 μm. Indeed, 6.2 μm PAH emission may be hidden in this broad plateau but the typical 7.7 and 8.6 μm are absent resulting in a decrease of the 7.7/11.2 ratio by roughly a factor of 10 compared to that of NGC0337. This is consistent with the atypical PAH emission in some low-luminosity active galactic nuclei (LLAGN) reported by Smith et al. (2007b).

The central spectrum exhibit silicate emission, blue continuum emission and fine-structure line emission of [NeII] at 12.8μm, [NeIII] at 15.5μm and [SIII] at 18.7μm (Figure 15, top). We adapted PAHFIT so that it includes Gaussian profiles to represent the silicate emission and used this modified PAHFIT to fit the continuum emission of both star light and dust towards the nucleus (Figure 15, top). While the silicate emission is not well fitted due to its asymmetry, the underlying continuum is well represented by the PAHFIT results. To characterize the silicate emission profile, we compared the continuum-subtracted silicate profile with the silicate absorption profile of the Galactic centre (Chiar & Tielens 2006) as well as the silicate emission profile observed towards the type 1 (i.e., face-on) LINER nucleus of

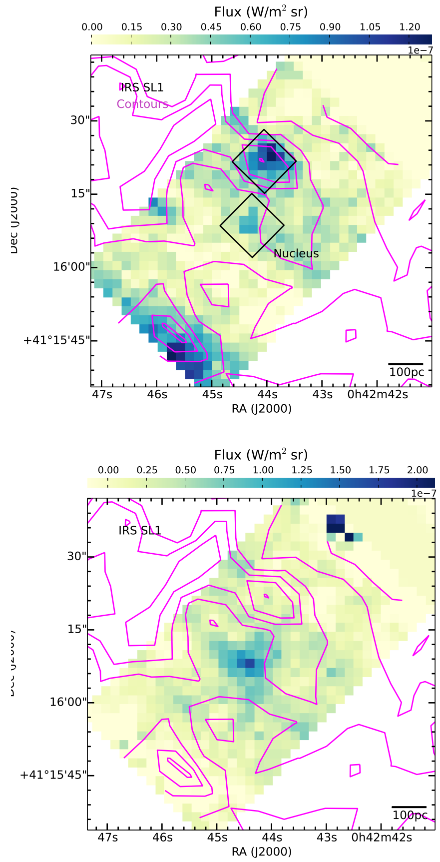

Figure 13. Integrated strength of the 11.2 μm PAH emission (left panel) and the silicate emission (from 9 to 11 μm, continuum subtracted; right panel) around the nucleus of M31. The two black boxes in the left panel are the $15'' \times 15''$ sub-apertures (centre and north region) used to extract spectra. The small white circle in the right panel shows a position halfway between the two components of the nucleus; these components are separated by 0$''$.5, which is well below the IRS spatial resolution. The contours in the right panel indicate the distribution of 3.6 μm luminosity in the same region, indicating the orientation of the M31 bulge.

M81 (Smith et al. 2010, Figure 15, bottom). For the latter, we adopted a spline continuum anchored at 8.36, 8.83, 24.7, 26.45, and 27.79 μm (Figure 15, middle). Compared to the silicate absorption profile towards the Galactic centre, the M31 silicate emission is clearly displaced towards longer wavelengths and the red wing is slightly less steep resulting in a slightly broader profile. This is consistent with previous results reporting that the silicate emission towards the M81 nucleus as well as towards several galaxies is redshifted and broader than the silicate absorption seen towards galactic sources (e.g. Sturm et al. 2005, 2006; Netzer et al. 2007; Smith et al. 2010). Contrasting the spectral properties of the nuclei of M31 and M81, we find that the "9.7" μm silicate emission is distinct from each other in peak position (9.9 and 10.56 μm respectively) and FWHM (2.58 and 2.79 μm respectively).[4] Moreover, the physical size of the sili-

[4] The reported FWHM is smaller than that reported by Smith et al. (2010) as we consider the continuum-subtracted silicate emission profile.

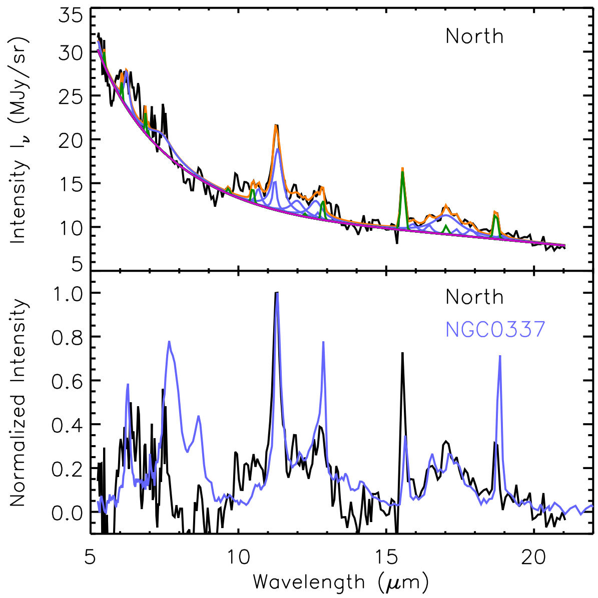

Figure 14. Top: PAHFIT result for the extracted spectrum from the north region of the M31 nucleus: fit (orange), continuum (magenta), individual dust components (blue), individual fine-structure lines and H_2 lines (green). Bottom: Continuum subtracted spectrum of the north region compared with that of the HII-type galaxy NGC0337 (Smith et al. 2007b), normalized to the peak intensity of the 11.2 μm PAH emission. PAH emission is clearly present longward of 10 μm.

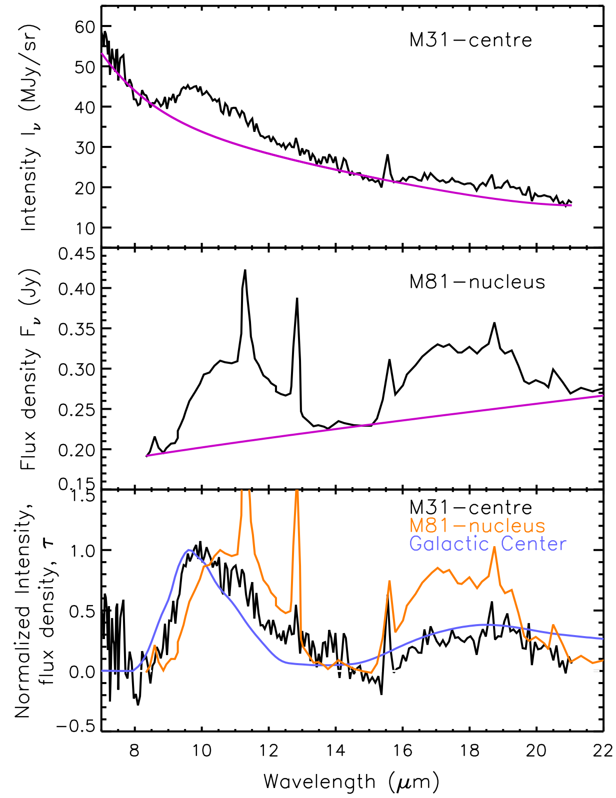

Figure 15. Top: Mid-infrared spectrum from the centre region of the M31 nucleus (black) with continuum (magenta). Middle: Mid-infrared spectrum of the nucleus of M81 (13″×13″aperture Smith et al. 2010, black) with continuum (magenta). Bottom: Normalized continuum-subtracted spectra of the M31 and M81 nuclei. For reference, the silicate optical depth profile towards the galactic centre is shown in blue (Chiar & Tielens 2006).

cate emitting region is much smaller in M31 (19–27pc with respect to 230pc for M81). And while M31 has no PAH emission in its nuclear centre, PAH emission is present across the nuclear region in M81. However, it is atypical in the same way as the PAH emission seen 15” North of M31's nuclear centre. Finally, also the atomic lines (e.g. [Ne II] 12.8 μm) are distinct between both nuclei.

Figure 16 compares the full 30″× 50″ M31 nuclear spectrum with the spectra extracted from the smaller regions in the centre and the North (inset, top and bottom). Also shown are nuclear spectra from six SINGS galaxies with similar spectral shapes (Smith et al. 2007b).[5] Some SINGS galaxies share similar PAH feature characteristics to the M31 spectrum and none of them contains obvious silicate emission. Although Mason et al. (2012) reported silicate emission towards NGC4594. All of these comparison galaxies have some type of LLAGN. The SINGS galaxies with similar spectral shapes include three elliptical galaxies, two spirals, and a lenticular; there is some disagreement over the exact nuclear spectral types of these six galaxies (Kennicutt et al. 2003; Smith et al. 2007b; Moustakas et al. 2010). All are classified as some form of LLAGN such as Seyfert or LINER (luminous AGNs were intentionally omitted from the SINGS sample; Kennicutt et al. 2003), although they are by no means the only LLAGNs in the SINGS sample. Published estimates of the black hole masses for these galaxies range from $1.5-5.5\times10^8$ M$_\odot$ (Nowak et al. 2008; Kormendy 1988, for NGC 1316 and NGC 4595, respectively), or about $1-4\times$ that of M31. M81 is classified as a LINER, with a black hole mass of 7×10^7 M$_\odot$ (Devereux et al. 2003). Li et al. (2009) concluded that the central black hole in M31 (M31*) is currently inactive, with direct observational signatures seen only at radio and X–ray wavelengths, so finding additional signatures in the mid-infrared is of great interest. To our knowledge, no such signatures have been reported; broadband mid-infrared imaging of the central regions of M31 (Davidge et al. 2006; Barmby et al. 2006) did not identify unambiguous nuclear emission. The bluest part of the spectrum in Figure 16 is dominated by the continuum, in agreement with the expectation that stellar light dominates the nucleus at these wavelengths.

Could radiation from M31* be responsible for the suppression of the 6–8 μm PAH features compared to the 11.3 μm feature? As discussed by Smith et al. (2007b) and Smith et al. (2010), inferring such a suppression must be done with caution, because the 6–8 μm features are more susceptible to dilution by the stellar continuum. Several connections between PAH suppression and the presence of an AGN are possible, including destruction of small PAH molecules by a hard radiation field, modification of the structure of the PAH molecules, or weak ultraviolet continuum from low star formation rates leading to decreased PAH ex-

[5] The IRS spectra for the SINGS galaxies were extracted over areas ranging from 2 to 8 kpc^2, whereas the M31 nucleus spectrum covers a much smaller area (0.02 kpc^2).

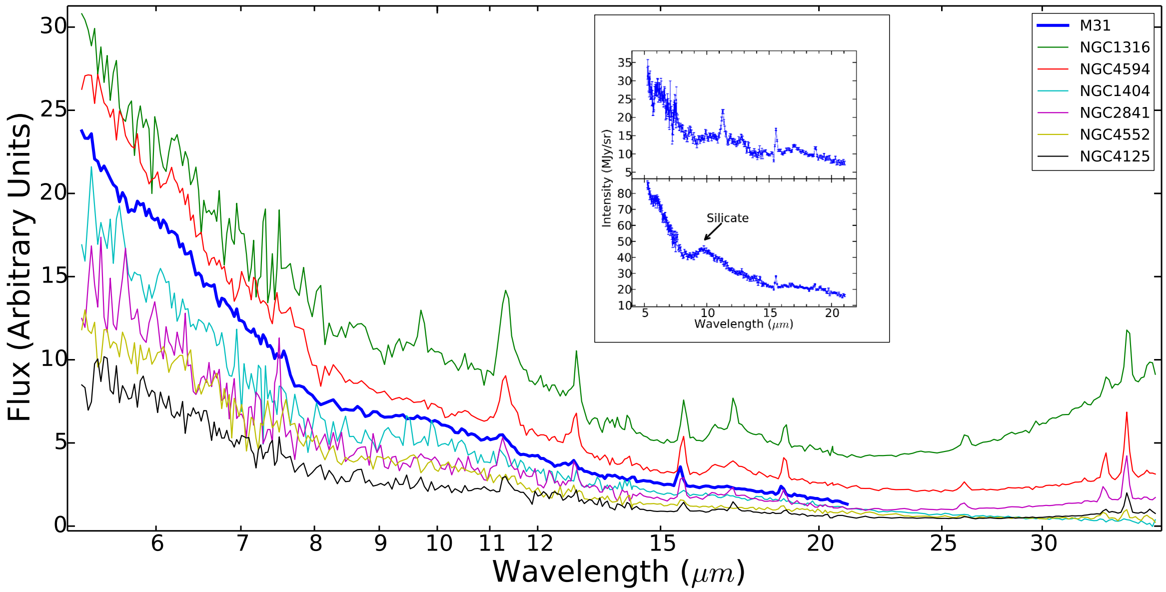

Figure 16. Mid-infrared spectrum of the nucleus of M31 (blue) over-plotted with spectra extracted close to the nuclei of 6 nearby galaxies which have AGN activity (Smith et al. 2007b). NGC 4552, NGC 1404 and NGC 4125 are elliptical galaxies and NGC 4594 and NGC 2841 are spiral galaxies. NGC 1316 is a lenticular galaxy. The inset shows the spectra extracted from the centre region of the M31 nucleus (bottom) and from the north region (top) shown in Figure 13.

citation (Smith et al. 2007b; Diamond-Stanic & Rieke 2010). In the latter case, the AGN is not the cause of the suppressed 6–8 μm features but rather is only detectable when the nuclear star formation rate is low. Previous work has found low rates of star formation in the centre of M31: although Melchior & Combes (2013) found a significant amount of cold gas in the centre of the galaxy, this gas does not appear to be associated with current star formation (see also Li et al. 2009). In modelling the far-infrared spectral energy distribution, Groves et al. (2012) found that the old stellar population in the M31 bulge is sufficient to heat the observed dust; no young stellar population is needed. We conclude that PAH feature ratios cannot provide direct evidence for radiation from M31*.

Detection of silicate emission in the M31 nuclear spectrum is another possible indicator of nuclear accretion. Silicate emission is not very common in integrated spectra of galaxies (Spoon et al. 2007) but is seen in luminous quasar spectra (e.g. Hill et al. 2014) and, as mentioned above, in the spectrum of the M81 nucleus. In the unified model of AGNs, an obscuring torus viewed face-on would be expected to show silicate emission (Efstathiou & Rowan-Robinson 1995; Spinoglio & Malkan 1992); however such a view would also be expected to show forbidden atomic lines such as [Ne V] and [S IV], not seen in the M31 spectrum. Alternatively, Mason et al. (2012) explained that low-luminosity AGNs cannot host a Seyfert-like obscuring torus because of their optically thin dust and low dust-to-gas ratio, but can show silicate emission that originates in the optically thin hot dust around the central engine. The first detection of such silicate emission was reported by Sturm et al. (2005) from the low-ionization nuclear emission-line region (LINER) galaxy NGC 3998, and Mason et al. (2012) observed that 9.7 μm silicate emission is present in many LLAGNs. To quantify the magnitude of the silicate emission in mid-infrared spectra, Smith et al. (2010) defined the linear slope parameter $\gamma 810 = [F_\nu(10\mu\text{m}) - F_\nu(8\mu\text{m})]/2F_\nu(9\mu\text{m})$, with positive values signifying silicate emission and negative values absorption. They found the M81 nucleus to have $\gamma 810 = 0.37 \pm 0.04$. For the M31 centre ($9'' \times 9''$) spectrum, we computed $\gamma 810 = 0.01 \pm 0.03$, indicative of neither absorption nor emission. However, for the continuum-subtracted spectrum, we measured $\gamma 810 = 1.6 \pm 0.4$. This combined with the similar characteristics of the silicate profile in M31 and M81, gives a much stronger indication that silicate emission is detected from M31*.

6 SUMMARY AND CONCLUSIONS

We obtained *Spitzer*/IRS spectral maps of 12 regions within M31 covering wavelengths 5–21 μm. The spectra from those regions, except for the nucleus, are similar to spectra obtained from other nearby star-forming galaxies. Early ISOCAM observations towards 4 regions of M31 showing a suppression of the 6–8 μm features' strength and an enhancement of the 11.3 μm feature intensity and FWHM (Cesarsky et al. 1998) were likely affected by the background subtraction methods applied.

We recover the well-known strong correlation between the 6.2/11.2 and 7.7/11.2 μm PAH intensity ratios that is governed by the PAH charge balance. This is another indicator that the PAH emission in all regions but the nucleus is typical. The PAH EQWs in M31 regions show a decreasing trend with increasing radiation hardness, consistent with previous results from other nearby galaxies. The distribution of PAH EQWs with metallicity is well within the range of the starburst galaxy sample of Engelbracht et al. (2008). We did not have enough data from low-metallicity regions of M31 to observe the decreasing trend of EQWs at low metallicities which is visible in other galaxies.

Different spectral features (11.2 μm PAH emission, [NeIII] 15.5 μm line emission, silicate emission) show distinct spatial distributions in the nuclear region. Mid-infrared spectra from near the nucleus of M31 show either suppressed 6–8 μm features and a strong 11.3 μm feature (15″off-nucleus) or silicate emission around 9.7 μm (on-nucleus). The silicate emission profile is redshifted and broader than that observed towards the Galactic centre, in line with previous results from other galaxies and the M81 nucleus. We contrast the spectral properties of the nuclei of M31 and M81 and find differences in the peak position and FWHM of the silicate feature, the silicate emitting region, the PAH emission, and the fine-structure line emission. The nuclear spectrum is similar to that of six other nearby galaxies known to have low luminosity AGN activity. This could strengthen the suggestion by Smith et al. (2007b) that low $L(7.7\mu\mathrm{m})/L(11.3\mu\mathrm{m})$ is an indicator of low luminosity AGN. The nuclear silicate emission is another possible AGN indicator. The 12 μm luminosity can be used to estimate a bolometric luminosity for the M31 nucleus of 1.6×10^{40} erg s^{-1}, well within the 'low-luminosity' classification, but well above the value estimated from the X–ray flux.

ACKNOWLEDGEMENTS

The authors thank D. Stock, K. Sandstrom and S. Lianou for fruitful discussions and technical support and S. Gallagher for helpful comments. We acknowledge support from NSERC Discovery Grants to PB and EP, an NSERC Discovery Accelerator Grant to EP, and JPL RSAs # 1369565 and 1279141 to HS. This work is based on observations made with the *Spitzer* Space Telescope, which is operated by the Jet Propulsion Laboratory, California Institute of Technology under a contract with NASA. This research has made use of NASA's Astrophysics Data System. The version of the ISO data presented in this paper correspond to the Highly Processed Data Product (HPDP) set called 'Mid-IR Spectro Imaging ISOCAM CVF Observations' by Boulanger et al. (2005), available for public use in the ISO Data Archive.

REFERENCES

Allamandola L. J., Tielens A. G. G. M., Barker J. R., 1989, ApJS, 71, 733
Bacon R., Emsellem E., Combes F., Copin Y., Monnet G., Martin P., 2001, A&A, 371, 409
Barmby P., et al., 2006, ApJ, 650, L45
Beirão P., Brandl B. R., Devost D., Smith J. D., Hao L., Houck J. R., 2006, ApJ, 643, L1
Bender R., et al., 2005, ApJ, 631, 280
Boulanger F., et al., 2005, A&A, 436, 1151
Brandl B. R., et al., 2006, ApJ, 653, 1129
Calzetti D., et al., 2010, Conference Proceedings 'Reionization to Exoplanets', ed. P. Ogle, ASP Conference Series,
Cesarsky C. J., et al., 1996, A&A, 315, L32
Cesarsky D., Lequeux J., Pagani L., Ryter C., Loinard L., Sauvage M., 1998, A&A, 337, L35
Chiar J. E., Tielens A. G. G. M., 2006, ApJ, 637, 774
Croley M., Barmby P., Stock D., Azimlu M., Rosolowsky E., 2014, MNRAS, submitted
Davidge T. J., Jensen J. B., Olsen K. A. G., 2006, AJ, 132, 521
Devereux N., Ford H., Tsvetanov Z., Jacoby G., 2003, AJ, 125, 1226
Diamond-Stanic A. M., Rieke G. H., 2010, ApJ, 724, 140
Efstathiou A., Rowan-Robinson M., 1995, MNRAS, 273, 649
Engelbracht C. W., Rieke G. H., Gordon K. D., Smith J.-D. T., Werner M. W., Moustakas J., Willmer C. N. A., Vanzi L., 2008, ApJ, 678, 804
Galliano F., Madden S., Tielens A., Peeters E., Jones A., 2008a, ApJ, 679, 310
Galliano F., Madden S. C., Tielens A. G. G. M., Peeters E., Jones A. P., 2008b, ApJ, 679, 310
Garcia M. R., et al., 2010, ApJ, 710, 755
Geballe T. R., Lacy J. H., Persson S. E., McGregor P. J., Soifer B. T., 1985, ApJ, 292, 500
Gillett F. C., Forrest W. J., Merrill K. M., 1973, ApJ, 183, 87
Gordon K. D., et al., 2006, ApJ, 638, L87
Gordon K. D., Engelbracht C. W., Rieke G. H., Misselt K. A., Smith J.-D. T., Kennicutt Jr. R. C., 2008, ApJ, 682, 336
Groves B., et al., 2012, MNRAS, 426, 892
Hao L., et al., 2005, ApJ, 625, L75
Hill A. R., Gallagher S. C., Deo R. P., Peeters E., Richards G. T., 2014, MNRAS, 438, 2317
Hony S., Van Kerckhoven C., Peeters E., Tielens A. G. G. M., Hudgins D. M., Allamandola L. J., 2001, A&A, 370, 1030
Houck J. R., et al., 2004, ApJS, 154, 18
Hudgins D. M., Allamandola L. J., 2004, in Witt A. N., Clayton G. C., Draine B. T., eds, Astronomical Society of the Pacific Conference Series Vol. 309, Astrophysics of Dust. p. 665
Kennicutt Jr. R. C., et al., 2003, PASP, 115, 928
Kessler M. F., et al., 1996, A&A, 315, L27
Kormendy J., 1988, ApJ, 335, 40
Lauer T. R., et al., 1993, AJ, 106, 1436
Li Z., Wang Q. D., Wakker B. P., 2009, MNRAS, 397, 148
Li Z., Garcia M. R., Forman W. R., Jones C., Kraft R. P., Lal D. V., Murray S. S., Wang Q. D., 2011, ApJ, 728, L10
Madden S. C., 2000, New A Rev., 44, 249
Mason R. E., Levenson N. A., Shi Y., Packham C., Gorjian V., Cleary K., Rhee J., Werner M., 2009, ApJ, 693, L136
Mason R. E., et al., 2012, AJ, 144, 11
McConnachie A. W., Irwin M. J., Ferguson A. M. N., Ibata R. A., Lewis G. F., Tanvir N., 2005, MNRAS, 356, 979
Melchior A.-L., Combes F., 2013, A&A, 549, A27
Moustakas J., Kennicutt Jr. R. C., Tremonti C. A., Dale D. A., Smith J.-D. T., Calzetti D., 2010, ApJS, 190, 233
Muñoz-Mateos J. C., et al., 2009, ApJ, 703, 1569
Nagao T., Maiolino R., Marconi A., 2006, A&A, 459, 85
Netzer H., et al., 2007, ApJ, 666, 806
Nowak N., Saglia R. P., Thomas J., Bender R., Davies R. I., Gebhardt K., 2008, MNRAS, 391, 1629
Pagani L., Lequeux J., Cesarsky D., Milliard B., Lionard L., Sauvage M., 1999, A&A, 351, 447
Peeters E., 2011, in IAU Symposium. pp 149–161, `arXiv:1111.3680`, doi:10.1017/S174392131102494X

Puget J. L., Leger A., 1989, ARA&A, 27, 161
Roche P. F., Aitken D. K., Smith C. H., Ward M. J., 1991, MNRAS, 248, 606
Sanders N. E., Caldwell N., McDowell J., Harding P., 2012, ApJ, 758, 133
Sandstrom K. M., et al., 2012, ApJ, 744, 20
Skillman E. D., Terlevich E., Terlevich R., 1998, Space Sci. Rev., 84, 105
Smith J.-D. T., et al., 2007a, PASP, 119, 1133
Smith J.-D. T., et al., 2007b, ApJ, 656, 770
Smith H. A., et al., 2010, ApJ, 716, 490
Spinoglio L., Malkan M. A., 1992, ApJ, 399, 504
Spinoglio L., Malkan M. A., Rush B., Carrasco L., Recillas-Cruz E., 1995, ApJ, 453, 616
Spitzer Science Center 2012, Spitzer Data Analysis Cookbook, v5.0.1 edn. SSC, Pasadena, CA
Spoon H. W. W., Marshall J. A., Houck J. R., Elitzur M., Hao L., Armus L., Brandl B. R., Charmandaris V., 2007, ApJ, 654, L49
Stock D. J., Peeters E., Tielens A. G. G. M., Otaguro J. N., Bik A., 2013, ApJ, 771, 72
Sturm E., et al., 2005, ApJ, 629, L21
Sturm E., et al., 2006, ApJ, 653, L13
Tielens A. G. G. M., 2008, ARA&A, 46, 289
Vermeij R., Peeters E., Tielens A. G. G. M., van der Hulst J. M., 2002, A&A, 382, 1042
Werner M. W., et al., 2004, ApJS, 154, 1

This paper has been typeset from a TEX/ LATEX file prepared by the author.